ENGINEERING Information Technology & Electronic Engineering
https://www.academax.com/EITEE; https://www.engineering.org.cn
https://ieeexplore.ieee.org/xpl/RecentIssue.jsp?punumber=11344065
E-mail: eng.itee@zju.edu.cn

Engineering Journals
Available on IEEE Xplore®

Research Article
https://doi.org/10.1631/ENG.ITEE.2026.0117

Design and hardware implementation of bio-inspired neural synchronization anti-interference circuits

Chaojun CHEN, Shutong CHEN, Yun MA, Junxi ZHU, Chenxi ZHAO, Quanlin GUO, Dezhi GOU✉

School of Electronic Information Engineering, China West Normal University, Nanchong 637009, China

Abstract: Conventional circuit systems typically exhibit limited capability in suppressing disturbances with strong temporal structures. This study proposes a bio-inspired anti-interference framework based on neural synchronization mechanisms. Hodgkin–Huxley (HH) and Izhikevich (IZH) networks with different topologies are compared in terms of synchronization stability, energy deviation, and hardware feasibility under external interference. The proposed framework integrates the neuron models and topological structures of neural networks to establish a unified evaluation system for bio-inspired anti-interference circuits. The simulation results demonstrate that the HH network exhibits stronger robustness under strong coupling, maintaining a synchronization index near 1.0 and a lower relative energy deviation than the IZH network. The small-world topology achieves the best disturbance tolerance, whereas the chain topology exhibits the weakest robustness for both models. In addition, hardware implementation demonstrates that the IZH network significantly reduces lookup table consumption, and both the HH and IZH circuits maintain rhythmic firing and waveform integrity under 20 mV square-wave interference. These results indicate that neural synchronization mechanisms provide an effective and practically implementable mechanism for adaptive anti-interference circuit design.

Key words: Bio-inspired anti-interference; Neural synchronous dynamics; HH/IZH network models; Hardware implementation

1 Introduction

Bio-inspired electromagnetic protection has attracted increasing attention as an effective route for enhancing the robustness of electronic systems in complex interference environments (Liu SH et al., 2022). Unlike conventional protection methods that primarily rely on passive shielding, filtering, or fixed suppression strategies, biological systems maintain stable information processing under external perturbations via adaptive regulation, nonlinear feedback, and collective synchronization (Takahashi et al., 2022; Liu DH et al., 2023; Wu et al., 2023; Yuan et al., 2023). These mechanisms inspire circuit systems exposed to temporally structured disturbances, such as periodic pulse interference, recurrent switching noise, and rhythmically injected electromagnetic perturbations. These disturbances may repeatedly interact with the intrinsic operating rhythm of circuits, causing cumulative waveform distortion and degradation of dynamic stability. Therefore, exploring neural dynamics-based bio-inspired mechanisms is important for developing adaptive anti-interference circuits with enhanced stability and recovery capability.

✉ Dezhi GOU, gdz_scu@163.com
Chaojun CHEN, https://orcid.org/0009-0006-3915-9096
Dezhi GOU, https://orcid.org/0000-0002-4959-217X
CLC number: TP183

Received: Apr. 27, 2026; Revision accepted: June 22, 2026;
Crosschecked: July 9, 2026

Recent studies on neural circuits and synchronization have demonstrated that neuronal dynamics, energy regulation, synaptic coupling, and network topology are closely related to stability and robustness of neural systems. Ma (2023) reviewed biophysical neuron models, energy mechanisms, and synapse controllability, and emphasized that energy exchange and synaptic regulation are important for understanding the controllable behavior of neural systems. Zhang et al. (2026) investigated a heterogeneous cyclic Hopfield neural network without self-connections, and demonstrated that heterogeneous structures and cyclic connections enrich network dynamics and affect collective stability. Wang XQ et al. (2023) analyzed the effects of potassium channel blockage on inverse stochastic resonance in Hodgkin–Huxley (HH) neural systems, and indicated that ion channel dynamics significantly influence neuronal responses under external perturbations. Bossy et al. (2019) investigated the synchronization of stochastic mean-field networks of HH neurons with noisy channels, and proved that strong electrical interactions promote exponential synchronization under channel noise. Khoshkhou and Montakhab (2020) revealed that topology and synaptic interactions play an important role in synchronization transitions of spiking HH neural networks. These studies indicate that neural synchronization, energy-state evolution, synaptic coupling, and network topology are key factors influencing disturbance-tolerant neural behavior. However, their combined influence on bio-inspired anti-interference circuit design, especially under temporally structured disturbances, has not been systematically investigated.

Despite these advances, several key issues remain to be addressed. First, most existing studies focus on a single neuronal model,

making it difficult to determine whether anti-interference robustness primarily originates from detailed biophysical dynamics or simplified spiking mechanisms (Peng et al., 2024; Zhao et al., 2024; Lin et al., 2025). Second, the coupled effects of synchronization recovery, network topology, and energy-state variations under structured disturbances remain unclear (Guo et al., 2023; Wang B et al., 2025). Third, although field-programmable gate array (FPGA) and system-on-chip platforms provide feasible routes for real-time neural circuit implementation, the relationship between anti-interference performance, model complexity, and hardware resource consumption has not been systematically studied (Yu et al., 2023; Beaubois et al., 2024; Heidarpur et al., 2024).

To address these issues, this study proposes a bio-inspired anti-interference framework based on neural synchronization dynamics. The HH and Izhikevich (IZH) models are selected as two representative neuronal models with different levels of dynamical complexity. The HH model retains conductance-based biophysical feedback and multi-timescale ion channel dynamics, whereas the IZH model provides simplified spiking dynamics with lower computational complexity. Under the same stimulus, interference, coupling, and topology conditions, the two models are compared in terms of waveform preservation, rhythmic stability, synchronization recovery, energy-state variation, anti-interference reliability, and hardware feasibility. In addition, chain, ring, and small-world network topologies are constructed to investigate the influence of connectivity patterns on disturbance propagation and synchronization stability. An energy evaluation method is introduced to quantify variations in network energy states under interference. Furthermore, a time-division multiplexing (TDM) hardware implementation scheme is developed on an FPGA platform, and the hardware results are compared with simulation results to verify the accuracy and feasibility of the proposed framework.

The remainder of this paper is organized as follows: First, the theoretical basis of the proposed bio-inspired anti-interference framework is established, including the HH and IZH neuron models, the synaptic coupling mechanism, the energy indicators, and the network topology construction. Next, simulation studies are conducted to compare action potential characteristics, synchronization stability, energy characteristics, and anti-interference performance under different coupling strengths and topological structures. Subsequently, an FPGA-oriented implementation based on the TDM strategy is presented for hardware verification. Finally, the relationships among neuronal dynamics, network topology, energy-state preservation, anti-interference robustness, and hardware cost are discussed to provide guidance for the design of bio-inspired anti-interference circuits.

2 Theoretical basis and model construction of the bio-inspired anti-interference framework

2.1 Single-neuron anti-interference mechanism and equivalent model

2.1.1 Nonlinear robustness mechanism of the HH model

The HH model precisely describes the generation of action potentials through the dynamics of voltage-gated ion channels, and is a typical microscopic model for investigating the anti-interference characteristics of biological neurons (Hodgkin and Huxley, 1952). Mathematically, the HH model can be represented as follows:

$$C\frac{\mathrm{d}V_i}{\mathrm{d}t}=G_{\mathrm{Na}}m_i^3h_i\left(E_{\mathrm{Na}}-V_i\right)+G_{\mathrm{K}}n_i^4\left(E_{\mathrm{K}}-V_i\right)+G_{\mathrm{L}}\left(E_{\mathrm{L}}-V_i\right)+I_{\mathrm{syn}(i,j)}+I_{\mathrm{ext},i}, \tag{1}$$

$$\frac{\mathrm{d}m}{\mathrm{d}t}=\alpha_m(1-m)-\beta_m m, \tag{2}$$

$$\frac{\mathrm{d}h}{\mathrm{d}t}=\alpha_h(1-h)-\beta_h h, \tag{3}$$

$$\frac{\mathrm{d}n}{\mathrm{d}t}=\alpha_n(1-n)-\beta_n n, \tag{4}$$

where V_i represents the membrane potential of neuron i, C represents the capacitance of the cell membrane, and $I_{\mathrm{syn}(i,j)}$ denotes the synaptic transmission current received by neuron i from neuron j. $I_{\mathrm{ext},i}$ denotes the external input current applied to neuron i. In the absence of external stimulation, $I_{\mathrm{ext},i}$ is 0. G_{Na}, G_{K}, and G_{L} denote the maximum conductances of sodium, potassium, and leak channels, respectively. E_{Na}, E_{K}, and E_{L} denote the reversal potentials of sodium channels, potassium channels, and leak current respectively, which are caused by the concentration gradient of ions inside and outside the membrane. m_i represents the activation of the sodium channels of neuron i, h_i represents the inactivation of the sodium channels, and n_i represents the activation of the potassium channels. m and h represent the gating parameters of sodium ion channels, and n represents the gating parameter of potassium ion channels. The voltage-dependent rate functions α_m, β_m, α_h, β_h, α_n, and β_n determine the opening and closing dynamics of the corresponding ion-channel gates. Based on the coupling relationship between ion channels and their gating variables, the HH model can accurately describe the dynamic processes of membrane depolarization and repolarization.

Within this dynamical structure, the interaction between Na^+ and K^+ channels forms a self-limiting feedback loop that suppresses external transient disturbances (Schuman et al., 2022). Its threshold mechanism and refractory period prevent erroneous triggering and repetitive firing, endowing the model with inherent resistance to periodic or random interference. In addition, the nonlinear feedback acts as an adaptive damping mechanism that attracts and stabilizes perturbed trajectories in the phase plane. Therefore, the HH model reveals the anti-interference mechanism of neurons from a biophysical perspective, and provides a theoretical foundation for the engineering design of anti-interference neural networks. Fig. 1 shows the action potential waveform of the HH model.

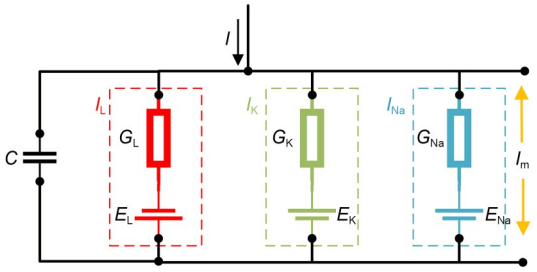

Fig. 1 Action potential of the HH model. I_{L}, I_{K}, and I_{Na} denote the leakage, potassium, and sodium ionic currents, respectively. E_{L}, E_{K}, and E_{Na} represent the corresponding reversal potentials, while I_{m} denotes the total ionic membrane current, given by $I_{\mathrm{m}}=I_{\mathrm{L}}+I_{\mathrm{K}}+I_{\mathrm{Na}}$

This study adopts typical parameter values of the HH model, and the values of each parameter are shown in Table 1.

Table 1 Typical parameters of the HH neural network model

Variable	Typical value	Unit
C	1	μF/cm^2
G_{Na}	120	mS/cm^2
G_K	360	mS/cm^2
G_L	0.3	mS/cm^2
E_{Na}	50	mV
E_K	−77	mV
E_L	−54.5	mV

2.1.2 Computational efficiency and dynamic adaptability of the IZH model

The neural dynamics model proposed by Izhikevich (2003) can precisely reproduce the rich and diverse discharge behaviors of biological neurons, and is suitable for neural network simulation. Mathematically, the IZH model can be expressed as follows:

$$\frac{dV}{dt}=0.04V^2+5V+140-U+I, \tag{5}$$

$$\frac{dU}{dt}=a(bV-U), \tag{6}$$

with the auxiliary after spike resetting

$$\text{if } V\geq V_{peak}, \text{ then } V\leftarrow c, U\leftarrow U+d, \tag{7}$$

where V represents the membrane potential of the neuron, U represents the membrane recovery variable characterizing the slow recovery effect associated with ionic activation and inactivation during the firing process, and I represents the scaled input to the neuron including external injected and synaptic inputs. The parameter a determines the time scale of the recovery variable U, and b describes the sensitivity of U to the membrane potential V. The parameter c represents the reset value of the membrane potential after spike firing, d represents the increment in the recovery variable after reset, and V_{peak} denotes the spike-peak threshold. In accordance with the conventional scaled formulation of the IZH model, V, U, I, V_{peak}, and the parameters a, b, c, and d are treated as dimensionless quantities. In the regular spiking mode adopted in this study, the parameter values are set as follows: a=0.02, b=0.2, c=−65, d=8, and V_{peak}=30.

As shown in Fig. 2, the negative feedback regulation of the recovery variable U effectively counteracts cumulative disturbances, ensuring that the system maintains stable oscillations even in the presence of interference. Its nonlinear reset mechanism suppresses numerical divergence and abnormal activation via periodic bounding, thereby achieving a balance between computational efficiency and dynamic robustness.

Therefore, the IZH model can not only implement the primary dynamic characteristics of neural discharge with low hardware resource requirements, but also exhibit anti-interference steady-state properties similar to those of the HH model. This provides an ideal engineering foundation for the anti-interference design of neural networks on platforms such as FPGA.

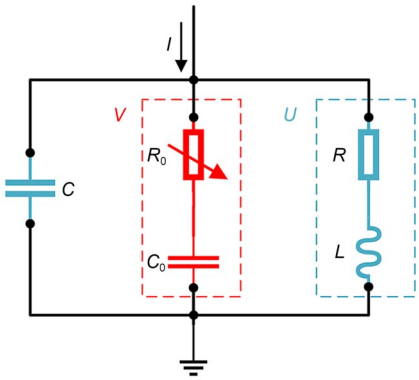

Fig. 2 Action potential of the IZH model. *I* denotes the external input current injected into the neuron circuit. R_0 denotes the nonlinear voltage-controlled resistance, and C_0 denotes the equivalent capacitance in the membrane-potential branch, which together reproduce the fast nonlinear dynamics of the membrane potential *V*. *R* and *L* denote the resistance and inductance in the recovery-variable branch, respectively, and determine the damping and dynamic response of the recovery variable *U*

2.2 Analysis of the anti-interference mechanism of neural network layers

2.2.1 Role of synapses in anti-interference

At the neural network level, the interaction between neurons is the key structural component for achieving anti-interference performance.

In biological systems, neurons primarily achieve signal transmission and modulation through synaptic transmission. The Leonid chemical synapse model can precisely describe the electrochemical coupling process between neurons, and accurately reproduce the propagation characteristics of action potentials in a highly realistic manner (Savtchenko, 2007).

In this study, the anti-interference mechanism of the network layer is accurately constructed based on the above synaptic coupling model.

We consider two neurons i and j that are coupled by the chemical synapses of Leonid. The coupling term is defined as follows:

$$I_{syn(i,j)}=I_{syn(Leonid)}, \tag{8}$$

$$I_{syn(Leonid)}=-C_m S_j\frac{\partial(V_i-V_j)}{\partial t}+G_s(V_p-E_s+V_i-V_j). \tag{9}$$

The Leonid model has achieved highly accurate transmission of neuronal action potentials. Here, $I_{syn(Leonid)}$ denotes the postsynaptic current; G_s denotes the postsynaptic conductance and the coupling strength between the neuron and synapse; V_p denotes the postsynaptic holding potential; E_s denotes the postsynaptic reversible potential; V_i and V_j denote the membrane potentials of the presynaptic neuron i and postsynaptic neuron j at the synapse, respectively; $-C_mS_j$ describes the capacitive current of the presynaptic neuron j, and the product of G_s and $V_p-E_s+V_i-V_j$ describes the ionic current flowing through the receptor-gated channels of the postsynaptic receptor. The values of each parameter are shown in Table 2.

The primary function of chemical synapses is not only signal transmission but also the reconfiguration of the disturbance propagation path in the network. When neuron j is subjected to external interference, the fluctuation of its membrane potential V_j acts on neuron i through synaptic current I_{syn}. Unlike linear coupling, the

Table 2 Parameters of the Leonid model

Variable	Typical value	Unit
C_m	1	μF/cm^2
S_j	0.001×2π	cm^2
G_s	1–10	mS/cm^2
V_p	−65	mV
E_s	−70	mV

nonlinear response function S_j of chemical synapses performs threshold selection and dynamic shaping on input signals. This action rapidly attenuates minor disturbances while effectively transmitting significant signals. This mechanism averages or eliminates disturbances during transmission, thereby forming a dynamic filtering effect and achieving adaptive allocation and steady-state regulation of disturbance energy.

2.2.2 Impact of topological characteristics on interference resistance

When multiple neurons are coupled through chemical synapses, the system achieves a nearly synchronous state under an appropriate coupling strength. In this state, although the membrane potentials of each neuron slightly differ, the discharge rhythms remain phase-locked. This quasi-synchronous behavior provides the system with a self-stabilizing working mode (Zhou et al., 2023). The interference is distributed and dissipated via synaptic interactions, forming the overall steady-state response of the network. This process manifests as a collective stabilization effect at the dynamical level. Specifically, multinode feedback loops suppress local disturbance amplification and maintain global potential stability, thereby forming the core dynamical basis for the anti-interference characteristics of the neural network layer.

Using the HH and IZH models as basic neuron units and synaptic transmission mechanisms as the network foundation, two types of neural networks have been designed. Both networks (HH and IZH) consist of 11 neurons and are configured into 10 topological structures by combining different connection methods. Among them, eight topologies refer to the construction rules of the Newman–Watts small-world network model and thus form irregular topological structures similar to the small-world network. Specifically, with neuron 1 (N1) as the center while maintaining the ordinal connections from N1 to N2 up to N11, N1 sequentially forms unidirectional couplings with all other nonconnected neurons through Leonid chemical synapses. By gradually increasing the long-range connection edges, 10 different ring-like irregular topological structures (chain, ring, topologies 1–8) are obtained. These networks maintain the local clustering property while shortening the average path length, thereby forming a feature similar to that of a "small world" (Soltani et al., 2024). Fig. S1 in the supplementary materials shows the 10 types of neural network topological structures.

In these networks, coupling between the N^{th} and $(N+1)^{th}$ neurons is achieved through Leonid chemical synapses (Fig. 3). The membrane potential V_i of the presynaptic neuron is transmitted to the postsynaptic neuron through the synaptic channel, generating a membrane potential response, V_j. The synaptic feedback pathway returns part of the electrical signal to the presynaptic neuron, forming a closed potential feedback loop. Notably, the direction of this synaptic

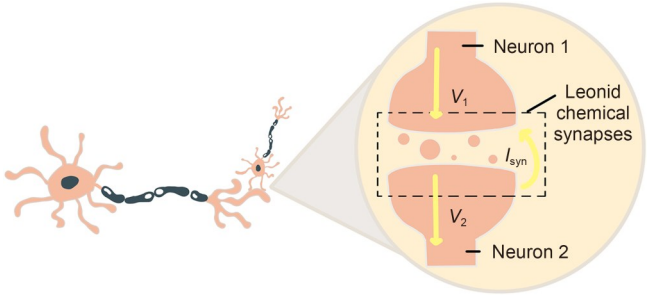

Fig. 3 Structure of the Leonid chemical synapses

connection is not completely symmetrical. The information primarily spreads from N1 to other neurons through the newly added unidirectional connections. However, the synaptic feedback current returns some signals to the upstream nodes, forming a local bidirectional but overall asymmetric information flow. This structural feature comprises long-range unidirectional connections and local feedback loops, which not only accelerate global phase synchronization but also enhance the dissipative capacity of local disturbances.

In addition, the nonlinear response function S_j of the Leonid chemical synapse exhibits a selective coupling characteristic: It rapidly suppresses small disturbances and effectively transmits significant signals, thereby forming a dynamic filtering effect in the network. This selective conduction and the structural characteristics of the small-world topology synergize to enable the network to achieve a balance between synchronicity and robustness.

2.3 Principles of neural dynamics generation on FPGA platforms

2.3.1 Discretization of the model equation and the mechanism for synchronous time update

Implementing continuous neural differential equations on an FPGA requires converting them into a discrete-time form. Typically, numerical methods such as forward Euler or RK4 are adopted. Considering the real-time performance and resource constraints of FPGAs, this study implements the approximate integration update within the time step using the following improved Euler method:

$$V_{k+1}=V_k+\Delta t\cdot f\left(V_k,m_k,h_k,n_k,I_k\right), \tag{10}$$

where V_k and V_{k+1} denote the membrane potentials at the k^{th} and $(k+1)^{th}$ time steps, respectively, k is the index of the discrete time step, Δt is the fixed simulation time step, m_k and h_k represent the activation and inactivation gating variables of the sodium channels, respectively, n_k represents the activation gating variable of the potassium channels, I_k denotes the total input current, and $f(\cdot)$ represents the membrane–potential derivative determined by the neuron model equations.

This method has a simple structure and controllable calculation delay; it is convenient for pipelining deployment. Through synchronous updates with a fixed step size, all neurons complete the state update at the same clock edge, thereby maintaining global time consistency at the physical level and providing a hardware foundation for network synchronous discharges.

2.3.2 Indicators for evaluating anti-interference performance

1. Synchronization index

In this study, the synchronization index is used as a key metric for data acquisition and processing to quantify the anti-interference strength of the network topology (Kazemi and Jamali, 2022). In the simulations, the number of neurons is denoted as N, and the simulation time T is divided into several small time windows τ. Within each time window, the firing sequences of any two neurons i and j are represented by $V_i(l)$ and $V_j(l)$ respectively, where the values of $V_i(l)$ and $V_j(l)$ are either 0 or 1. Here, l represents the number of specific time windows. The algorithm is as follows:

$$c_{ij}(t) = \frac{\sum_{l=1}^{m} V_i(l)V_j(l)}{\sqrt{\sum_{l=1}^{m} V_i^2(l)V_j^2(l)}}, \tag{11}$$

$$C = \frac{2}{N(N-1)} \sum_{i=1}^{N} \sum_{j=1, j\neq i}^{N} c_{ij}(\tau). \tag{12}$$

For $V_i(l)$ and $V_j(l)$, a value of 1 indicates that the neuron has generated an action potential discharge, whereas a value of 0 indicates no discharge. By calculating the discharge sequences of two neurons within each time window, the synchronization index between them can be obtained. The simulation time T is divided into m equal segments to accurately capture the dynamic behavior of the neural network. The resulting index values are usually limited within the range of 0–1, where a value closer to 1 indicates a higher degree of synchronization.

2. Reliability index

The concept of reliability evaluation is based on the approaches proposed by Mainen and Sejnowski (1995). They analyzed the consistency of neuronal firing patterns under various input conditions.

To quantitatively assess network stability under interference, a reliability index R is introduced based on the comparison between membrane potential sequences under normal and disturbed conditions. The reliability index is defined as follows:

$$R = 1 - \frac{\left\| V_{\mathrm{d}}(t) - V_{\mathrm{c}}(t) \right\|_2}{\left\| V_{\mathrm{c}}(t) \right\|_2}, \tag{13}$$

where $\left\| V_{\mathrm{d}}(t) - V_{\mathrm{c}}(t) \right\|_2$ denotes the 2-norm (Euclidean norm) of the difference between the disturbed membrane potential $V_{\mathrm{d}}(t)$ and the undisturbed membrane potential $V_{\mathrm{c}}(t)$. This norm represents the overall difference or "error energy" between the two signals. $\left\| V_{\mathrm{c}}(t) \right\|_2$ denotes the 2-norm of the membrane potential sequence $V_{\mathrm{c}}(t)$ under undisturbed conditions. An R value closer to 1 indicates stronger network stability. This study calculates the reliability index of N11 neuron.

3. Energy indicators

To quantitatively describe the dynamic-state evolution of the neural circuit under structured interference, an energy-like function is first defined based on the membrane potential dynamics. For neuron i, the instantaneous energy function is expressed as follows:

$$E_i(k) = V_i^2(k), \tag{14}$$

where $V_i(k)$ denotes the membrane potential of neuron i at the k^{th} sampling point.

The total activity energy of the network is then calculated as the time-averaged mean energy over all neurons and sampling points as follows:

$$E_N = \frac{1}{M} \sum_{k=1}^{M} E_i(k), \tag{15}$$

where N represents the number of neurons and M represents the total number of sampled points. This metric reflects the overall excitation level and dynamic activity intensity of the neural circuit during evolution.

To evaluate the impact of external interference, the relative energy deviation is also defined as follows:

$$\Delta E_N = \frac{\left| E_{N,\mathrm{d}} - E_{N,\mathrm{c}} \right|}{E_{N,\mathrm{c}}}, \tag{16}$$

where $E_{N,\mathrm{d}}$ and $E_{N,\mathrm{c}}$ denote the activity energy under disturbed and clean conditions, respectively. A smaller ΔE value indicates that the neural circuit better preserves its original dynamic state under structured disturbance, whereas a larger value implies greater vulnerability to interference.

In this study, the energy indicators, synchronization index, and reliability index are used to evaluate the anti-interference performance of different neural models and topological structures. This definition is widely adopted in spiking neural network analysis to characterize the global excitation state of systems.

3 Simulation results and discussion

To investigate the anti-interference function of the neural network, normal stimulation (a sinusoidal wave signal with an amplitude of 10 mV and a frequency of 0.1 rad/s) is applied to the N1 neuron, superimposed with an interference signal (with an amplitude of 20 mV, a period of 0.001 s, and a pulse width of 5% of a square-wave signal). The anti-interference function is evaluated using the synchronization and reliability indexes of the electrical potentials of each neuron in the network. This study performs analysis and comparison by varying the network structure and coupling strength G_{s} between neurons and synapses.

To determine whether the neural circuit exhibits effective discharge behavior under normal stimulation and interference, three complementary criteria are adopted in this study. The first criterion is waveform integrity, which evaluates whether the action potential preserves its basic depolarization, peak, and repolarization morphology after disturbance. The second criterion is rhythm preservation, which evaluates whether the firing sequence maintains stable inter-spike intervals and whether the dominant discharge rhythm remains continuous rather than being replaced by burst clustering or irregular compression. The third criterion is the network-level coordinated stability, which is evaluated using the synchronization and reliability indexes to determine whether the discharge pattern remains temporally consistent and resistant to disturbance propagation.

Based on these criteria, an effective discharge state is defined as a state in which the neuron or neural network preserves recognizable spike morphology, sustained rhythmic output, and stable inter-neuronal temporal coordination after interference injection. In contrast, if disturbance causes waveform distortion, abnormal spike

accumulation, severe rhythm compression, or unstable temporal alignment, the discharge effect is regarded as degraded.

3.1 Simulation model and action potential characteristics

The HH and IZH neural network models are established separately in the MATLAB/Simulink environment (Figs. S2 and S3). Both models are simulated under identical excitation conditions, identical disturbance parameters, and the same topology construction rules to ensure consistency in cross-model comparison. Figs. 4 and 5 show the action potential responses of the HH and IZH networks under different topologies, coupling strengths, and interference conditions, respectively.

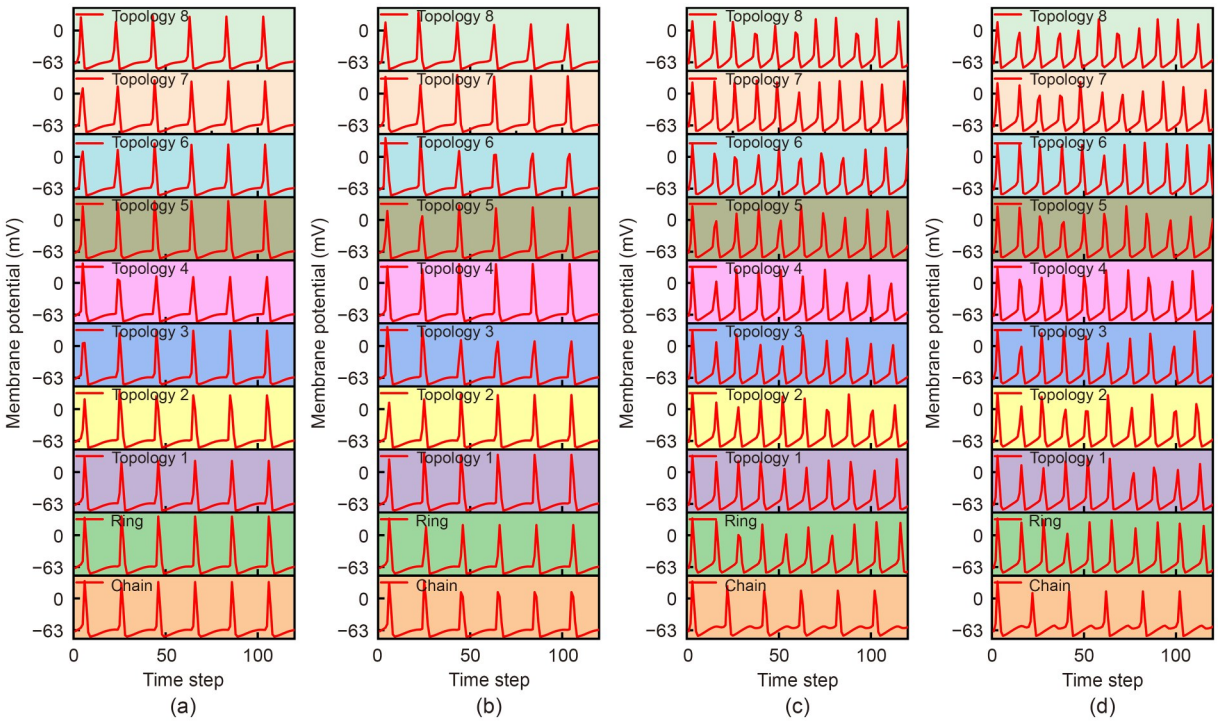

Fig. 4 HH model simulation results of the action potential diagram: (a) no signal interference when G_s=1 mS/cm^2; (b) under signal interference when G_s=1 mS/cm^2; (c) no signal interference when G_s=5 mS/cm^2; (d) under signal interference when G_s=5 mS/cm^2

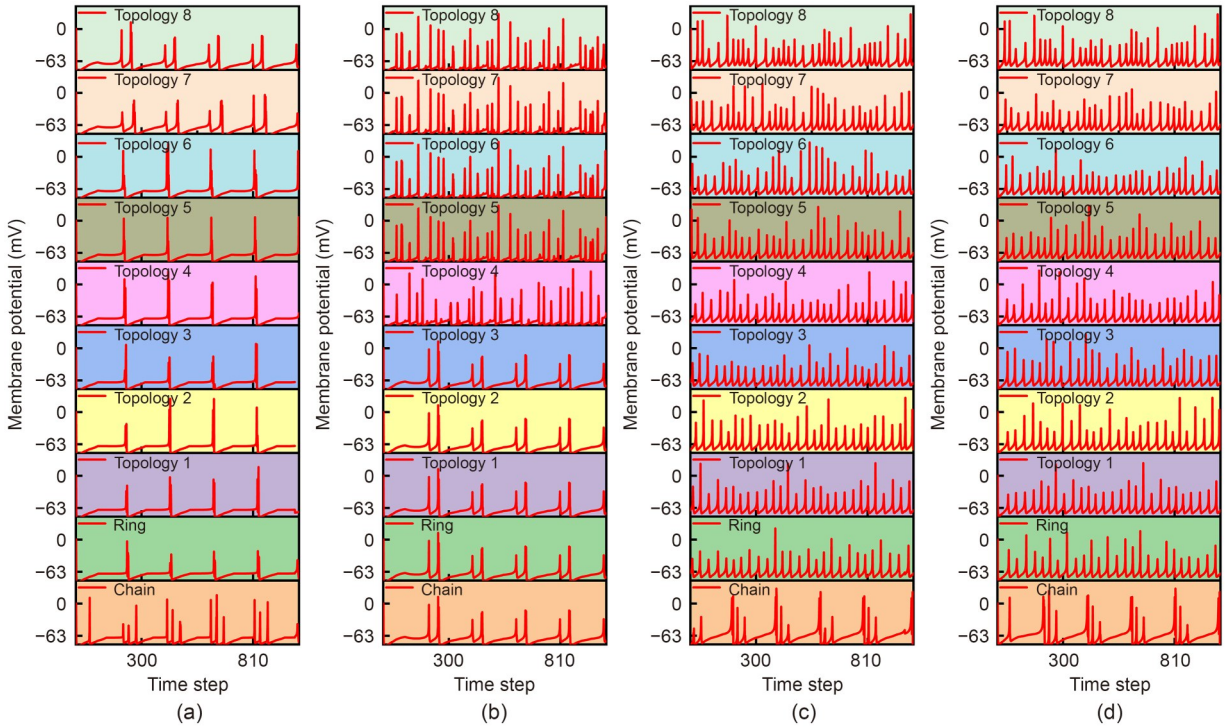

Fig. 5 IZH model simulation results of the action potential diagram: (a) no signal interference when G_s=1 mS/cm^2; (b) under signal interference when G_s=1 mS/cm^2; (c) no signal interference when G_s=5 mS/cm^2; (d) under signal interference when G_s=5 mS/cm^2

As shown in Fig. 4, the results of the HH network demonstrate that under weak coupling conditions (G_s=1 mS/cm^2), the principal spike positions and the overall firing rhythm remain largely unchanged before and after disturbance across different topologies. Although slight peak shifts and local timing perturbations are observed in some structures, the depolarization rising phase, spike peak formation, and repolarization process remain highly consistent. This indicates that the HH model possesses strong trajectory retention capability under external pulse disturbances. When the coupling strength increases to 5 mS/cm^2, the firing frequency of the HH network significantly increases, whereas the primary waveform morphology remains preserved. In particular, under small-world topologies, spike distributions become more uniform and variations in interspike intervals remain limited, demonstrating stronger rhythmic stability. These observations indicate that although the HH model is driven into a higher excitation state under strong coupling, the system still evolves around a stable limit cycle rather than entering a disordered regime.

In contrast, the IZH network exhibits significantly higher sensitivity to external input disturbances. Under weak coupling conditions, the IZH model maintains basic periodic firing before and after interference, as shown in Fig. 5. However, several topologies exhibit clear spike densification, characterized by increased spike counts and shortened interspike intervals, indicating a more direct response to disturbance injection. As the coupling strength increases, this phenomenon becomes more pronounced. Multiple topologies exhibit spike clustering, compressed firing rhythms, and localized burst accumulation at high frequencies. Although continuous firing is preserved, the action potential sequence transitions from regular periodic discharge to a firing pattern dominated by disturbance input. This suggests that under the combined effects of strong coupling and structured disturbance, the IZH model is more likely to enter a dynamic regime characterized by high excitation and reduced stability. In this regime, an increased spike count implies degraded rhythmic consistency rather than enhanced anti-interference capability.

Overall, these results indicate that the HH network maintains stronger waveform consistency and rhythmic stability under both weak and strong coupling conditions, with disturbance effects primarily manifested as minor phase deviations rather than structural distortion. In contrast, the IZH network exhibits higher sensitivity to external disturbances, with its firing behavior increasingly dominated by injected interference. Under strong coupling conditions, it transitions into a high-frequency but less stable response state. Therefore, from the perspective of action potential characteristics, the HH model exhibits superior trajectory retention capability, whereas the IZH model is more prone to rhythm compression and irregular firing patterns under disturbance.

3.2 Simulation results of synchronization behavior

To further quantify the collective coordinated behavior of the neural networks under structured disturbances, synchronization performance is analyzed from two perspectives. First, synchronization state action potential diagrams are used to observe spike timing alignment and phase locking behavior among neurons under different topologies. Second, the synchronization index and its variation rate after disturbance are used to quantitatively evaluate global synchronization stability. The former reflects the instantaneous alignment of rhythmic output during synchronous evolution, whereas the latter characterizes variations in overall phase consistency before and after interference injection.

Figs. S4 and S5 present the synchronization waveforms of the HH and IZH models under weak and strong coupling conditions across different topologies, respectively. In these figures, the red and blue curves represent the membrane potential trajectories of two representative neurons in the network, and their degree of overlap directly reflects synchronization quality.

In the HH network, under weak coupling conditions (G_s= 1 mS/cm^2), most topologies exhibit high synchronization quality, as shown in Fig. S4. In particular, in ring and small-world structures, the peak positions of the two neuronal curves almost coincide, with only slight phase deviations at a few spikes. This indicates that even under relatively weak coupling, the HH model maintains stable phase locking through its intrinsic multi-timescale feedback regulation. When the coupling strength increases to 5 mS/cm^2, the HH network exhibits markedly enhanced synchronization. In most topologies, the two waveforms nearly coincide, and the peak time difference approaches zero, indicating near-ideal global synchronization.

In contrast, the IZH network exhibits significantly different synchronization dynamics, as shown in Fig. S5. Under weak coupling conditions, although the IZH model achieves basic synchronization in some topologies, several structures exhibit obvious spike misalignment and local phase drift. This is particularly evident in chain and other sparsely connected topologies, where the spike timing deviation between neurons increases. This discrepancy becomes more pronounced as the coupling strength increases. Although the firing frequency increases significantly, many topologies exhibit excessive spike density, localized burst clustering, and layered peak misalignment. These results indicate that although the IZH network maintains high-frequency firing, stable phase consistency is lost. This suggests that under strong excitation, synchronization in the IZH model becomes vulnerable to overresponse instability rather than increasing linearly with stronger coupling.

The synchronization index and its variation rate confirm these observations, as shown in Figs. 6 and 7. Under weak coupling conditions, the IZH network achieves relatively high initial synchronization indices in some topologies because of its rapid threshold response. However, the variation rate after disturbance considerably

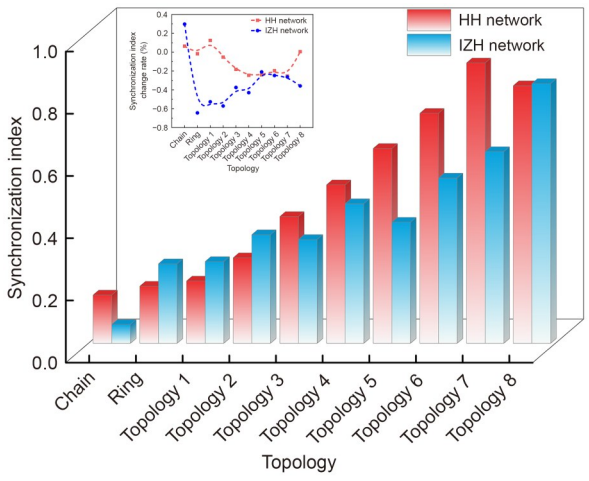

Fig. 6 Various types of synchronization indices and the rate of change due to interference when G_s=1 mS/cm^2

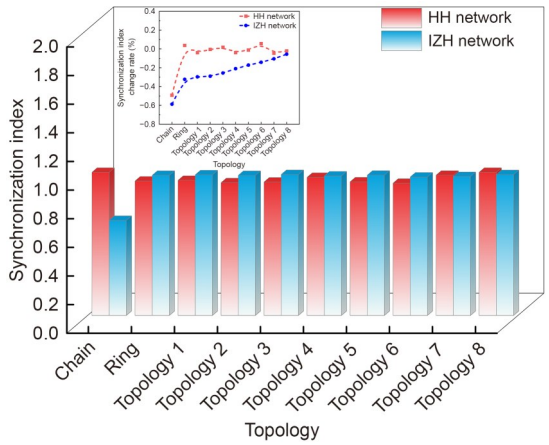

Fig. 7 Various types of synchronization indices and the rate of change due to interference when G_s=5 mS/cm^2

fluctuates, indicating that such synchronization lacks long-term stability. In contrast, although the HH network establishes synchronization slightly more slowly in the initial stage, the decrease in the synchronization index after disturbance is smaller. In particular, topology 8 exhibits the minimum synchronization variation rate, demonstrating the strongest resistance to phase drift.

When the coupling strength increases to G_s=5 mS/cm^2, the synchronization index of the HH network approaches unity across almost all topologies with a variation rate near zero, indicating that the network has reached a highly stable, globally phase-locked state. In contrast, although the IZH network maintains high-frequency firing under strong coupling, its synchronization indices decrease in several topologies, accompanied by a significantly larger variation rate. This implies that stronger coupling enhances excitation propagation but amplifies local timing mismatches, thereby reducing the overall phase consistency.

From the perspective of topology comparison, chain structures consistently exhibit the weakest synchronization performance for both models. Because signal transmission depends solely on sequential node-to-node propagation, local disturbances cannot be rapidly redistributed or corrected, resulting in cumulative phase errors. Ring structures partially address this problem through cyclic feedback, thereby enhancing synchronization stability. Small-world topologies perform best because their long-range shortcut connections significantly reduce the average path length, allowing locally induced phase deviations to spread rapidly throughout the network and be efficiently redistributed. Consequently, they exhibit the highest peak overlap in synchronization waveforms and the strongest stability in synchronization index measurements.

Collectively, the synchronization state diagrams and synchronization index analysis demonstrate that synchronization performance cannot be judged solely by instantaneous waveform overlap; instead, it must be evaluated by the variation rate of synchronization indices before and after disturbance. The former reflects local transient synchronization quality, whereas the latter reveals the global robustness of synchronization under interference. Based on this criterion, the HH model exhibits stronger synchronization stability under most topologies and coupling conditions, and the small-world topology consistently provides the optimal network structure for maintaining global synchronization performance.

3.3 Simulation results of anti-interference performance

This subsection evaluates the overall anti-interference performance of the neural networks based on the analysis results of action potential characteristics and synchronization behavior presented in Figs. S6–S8. The evaluation is performed from two perspectives: synchronization retention capability and reliability performance. A comprehensive comparison of synchronization indices, variation rates, and reliability values reveals obvious performance differences among different models, topologies, and coupling strengths. These quantitative results are highly consistent with the preceding waveform analysis of action-potential characteristics and synchronization behavior presented.

From the perspective of model comparison, under weak coupling conditions (G_s=1 mS/cm^2), the HH network significantly outperforms the IZH network overall. As shown in Fig. S8, the reliability values of the HH model range from 0.720 27 to 0.881 98, whereas those of the IZH model range only from 0.716 33 to 0.803 80. In particular, the HH network reaches a reliability value of 0.849 29 in topology 8, which is among the highest under weak coupling conditions. In combination with the data presented in Fig. S6, the synchronization indices of the HH network decrease slightly after disturbance in most topologies, and the synchronization variation rates remain close to zero, with slight positive changes in some cases. In contrast, the synchronization variation rates of the IZH network decrease substantially across all topologies, ranging from −0.2102 to −0.6447. This indicates that although the IZH model maintains high firing activity, its synchronization stability is significantly weaker.

When the coupling strength increases to 5 mS/cm^2, the performance gap between these two models increases. Under strong coupling conditions, the HH network maintains high reliability, with values ranging from 0.530 02 to 0.909 42 and the maximum value reaching 0.909 42, indicating that the HH model preserves stable output even under strong disturbance conditions. Fig. S7 shows that the synchronization indices of the HH model exceed 0.92 in most topologies and approach 1.0 in several topologies, demonstrating that the network remains in a highly coherent, globally synchronized state. In contrast, the reliability of the IZH network decreases significantly under strong coupling, ranging from 0.484 73 to 0.627 34. In several topologies, the synchronization variation rates decline to between −0.1056 and −0.5873, indicating that increased coupling intensifies rhythm instability rather than improving the network disturbance resistance.

From the perspective of network topology, small-world structures consistently exhibit the best performance under all conditions. As shown in Figs. S6–S8, in small-world topologies such as topologies 5, 7, and 8, both models achieve higher synchronization retention and reliability than in chain and ring structures. The HH model performs best in topology 8, where it not only achieves the highest reliability value of 0.849 29 but also exhibits an almost zero synchronization variation rate of +0.0051, indicating that it is nearly unaffected by disturbance. In contrast, chain structures consistently show the weakest performance. For example, under weak coupling conditions, in chain structures, the synchronization variation rate of the IZH model decreases to −0.2970, which is the largest degradation among all topologies. This demonstrates that disturbances

are more likely to accumulate and amplify in single-path propagation structures, thereby weakening the overall anti-interference capability.

3.4 Analysis of energy indicators

To evaluate the influence of structured disturbance on neural networks, the energy indicators defined in Eqs. (15) and (16) are calculated under different topologies and coupling strengths. The corresponding activity energies under weak and strong coupling conditions are shown in Figs. S9 and S10, respectively. The relative energy deviation is shown in Fig. 8.

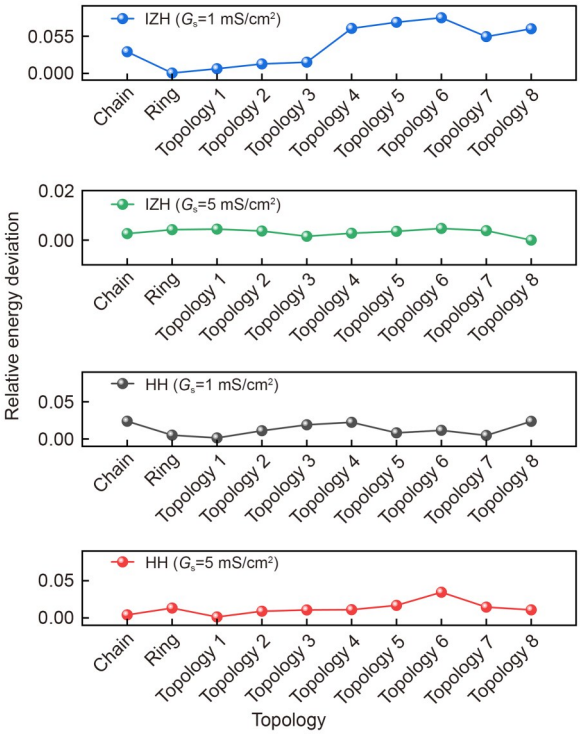

Fig. 8 Relative energy deviation of HH and IZH networks under different topologies and coupling strengths

As shown in Fig. S9, the activity energy of the HH network changes slightly before and after disturbance under both weak and strong coupling conditions, indicating that its overall activity level remains stable. In contrast, the IZH network exhibits more significant variations in activity energy under weak coupling, particularly in several small-world topologies, whereas the activity energy remains relatively close before and after disturbance under strong coupling.

The relative energy deviation shown in Fig. 8 confirms these results. For the HH network, the relative energy deviation remains within 0.001 384–0.023 751 and 0.001 240–0.034 512 under G_s=1 and 5 mS/cm^2, respectively, indicating strong dynamic-state preservation under disturbance. For the IZH network, the relative energy deviation ranges from 0.000 467 to 0.082 360 under weak coupling and from 0 to 0.004 723 under strong coupling, demonstrating stronger topology dependence, particularly under weak coupling conditions.

Overall, the energy indicator results demonstrate that the HH model preserves its original dynamic state more effectively under structured disturbance, whereas the IZH model is more sensitive to topology changes and interference. In general, topologies with smaller relative energy deviation tend to maintain the dynamic state more effectively after disturbance, even though the specific ranking is not always identical to that of synchronization or reliability indicators. These results indicate that anti-interference performance is influenced by the interaction between intrinsic neuronal dynamics, coupling behavior, and network topology.

3.5 Discussion on anti-interference mechanism

This subsection evaluates the overall anti-interference performance of the neural networks based on the analysis results of action potential characteristics, synchronization behavior, and energy indicators presented through simulation results. The evaluation is performed from three perspectives: synchronization retention, reliability performance, and dynamic-state preservation. A comprehensive comparison of synchronization indices, reliability values, and energy-indicator results reveals performance differences among different models, topologies, and coupling strengths.

From the perspective of model comparison, the HH network significantly outperforms the IZH network under both weak and strong coupling conditions. Under weak coupling (G_s=1 mS/cm^2), the HH model maintains smaller synchronization variation rates and higher reliability than the IZH model in most topologies. The energy-indicator results presented in Figs. 8 and S9 demonstrate that the HH network exhibits a small relative energy deviation, indicating that its dynamic state is slightly affected by structured disturbance. In contrast, the IZH model exhibits greater fluctuations in both synchronization and energy indicators, implying a higher sensitivity of the output state to interference.

When the coupling strength increases to G_s=5 mS/cm^2, the performance difference between these two models becomes more evident. The HH network maintains high synchronization indices, strong reliability, and small energy deviation in most topologies, demonstrating its strong anti-interference capability. In contrast, although the IZH network maintains a comparable activity level after disturbance, its synchronization degradation and reliability reduction are more pronounced. This indicates that for the IZH model, preservation of activity magnitude does not always imply stable temporal coordination under structured disturbance.

From the perspective of topology, chain structures generally exhibit weaker anti-interference performance because disturbances are more likely to accumulate along the sequential transmission path. Ring and small-world topologies perform better overall because they enable a more effective redistribution of disturbance effects and improve synchronization recovery. In particular, several small-world topologies exhibit small synchronization degradation, high reliability, and limited energy deviation with the HH model, indicating that these structures are more favorable for maintaining stable dynamic behavior under interference.

Overall, the anti-interference performance indicators demonstrate that the HH network achieves stronger waveform preservation, synchronization stability, reliability, and dynamic-state preservation than the IZH network under structured disturbance. The energy-indicator results provide an additional quantitative basis for evaluating anti-interference behavior, complementing the synchronization and reliability indices. These results confirm that the anti-interference capability of bio-inspired neural networks depends jointly on neuronal dynamics, coupling strength, and network topology.

4 Hardware implementation and anti-interference verification of synchronous neural network circuits

4.1 Hardware modeling and implementation principles

To verify the engineering feasibility of the proposed neural synchronization anti-interference circuit, hardware mapping and experimental validation of the HH and IZH neural network models are performed on an Xilinx Zynq XC7Z020-CLG400 FPGA platform. Fig. S11 shows the overall digital signal processing (DSP)/FPGA implementation flow, which consists of four stages: discrete model construction, fixed-point DSP mapping, neural network architecture implementation, and FPGA hardware deployment.

1. The continuous-time neural dynamics are discretized using the forward Euler method, transforming the HH and IZH models into difference equations suitable for digital computation.

2. The discretized models are translated into the fixed-point DSP hardware, where adders, multipliers, registers, and lookup tables (LUTs) are employed to update the membrane potential, evolve the gating variables, and compute the synaptic coupling.

3. Neural network architecture implementation is performed. A TDM strategy is employed to perform neuron-level temporal scheduling, where only a limited number of neuron processing cores (neuron IPs) and synapse processing units (synapse IPs) are instantiated, whereas a global controller sequentially updates all neurons according to the network topology.

4. The design is synthesized and implemented using Xilinx Vivado, and the resulting bitstream is downloaded to the FPGA for real-time execution. The hardware output waveforms are captured using on-chip and external acquisition modules.

To validate correctness, the FPGA results are compared with simulation results under identical initial conditions, coupling strengths, and network topologies. The comparison demonstrates strong consistency in waveform characteristics, synchronization behavior, and energy variation trends for the HH and IZH models, confirming the correctness and feasibility of the proposed DSP/FPGA implementation.

Notably, the TDM strategy significantly reduces hardware resource consumption by replacing spatial parallelism with temporal multiplexing; however, it imposes constraints on network topology complexity. Therefore, ring and chain topologies are selected for hardware verification because of their regular connectivity patterns, which provide a practical trade-off between implementability and representativeness.

4.2 FPGA resource utilization and timing performance

The Vivado synthesis and implementation results are as follows: the ring HH network consumes approximately 41 944 LUTs and 212 DSPs, whereas the chain HH network consumes 41 681 LUTs and 212 DSPs. The ring IZH network consumes approximately 3210 LUTs and 198 DSPs, and the chain IZH network consumes 3176 LUTs and 198 DSPs. The high LUT utilization of the HH model results from its complex exponential approximations and multichannel gating logic, whereas the IZH model requires only linear and quadratic computations.

Static timing analysis verifies that all implementations satisfy the 100-MHz clock constraint with a minimum slack of 2.3 ns. The membrane potential update rate reaches approximately 10^4 iterations per second, achieving real-time performance for millisecond-scale neural dynamics.

The experimental system is shown in Fig. 9.

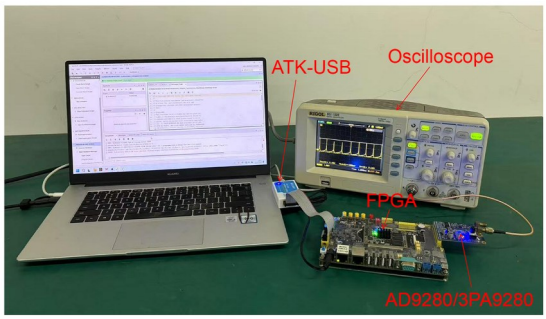

Fig. 9 Hardware experimental system diagram

4.3 Experimental results and analysis

To validate the synchronization and anti-disturbance performance, a direct digital synthesis module is implemented to inject a sinusoidal stimulus into neuron N1 with an amplitude of 10 mV and a frequency of 0.1 rad/s. For interference tests, a square-wave disturbance with an amplitude of 20 mV, a period of 0.001 s, and a duty cycle of 5% is superimposed on the input. The output signals are converted to analog voltages using an AD9280 or 3PA9280 analog-to-digital converter operating at 32 mega samples per second and captured using an oscilloscope. The measurement results are presented in Figs. S12 and 10.

4.3.1 Action potential test results

As shown in Fig. S12, under interference-free conditions, the ring and chain networks of the HH and IZH models exhibit stable periodic discharges. However, obvious differences are observed after introducing the square-wave disturbance. In the HH circuits, both ring and chain structures maintain regular action potential waveforms, with only slight phase shifts and minor frequency variations. Neurons such as N11 exhibit complete action potentials, indicating strong robustness against disturbance. In contrast, in the IZH circuits, although the ring structure maintains regular firing, the chain structure exhibits significant degradation after interference, including irregular spike timing, burst clustering, and waveform distortion, especially at downstream neurons such as N11.

4.3.2 Synchronization test results

The synchronization details are illustrated in Fig. 10. For the HH model, the action potentials of neurons N1 and N11 remain highly overlapped in both ring and chain structures, even after disturbance injection, demonstrating its strong phase-locking capability. In contrast, for the IZH model, synchronization strongly depends on the topology. In the ring structure, partial phase alignment is maintained; however, significant timing deviations exist. In the chain structure, the synchronization between N1 and N11 significantly degrades after disturbance, demonstrating obvious phase lag and loss of alignment.

4.3.3 Results of anti-interference performance indicators

The quantitative results presented in Table 3 support the above observations. Under interference-free conditions, the HH model

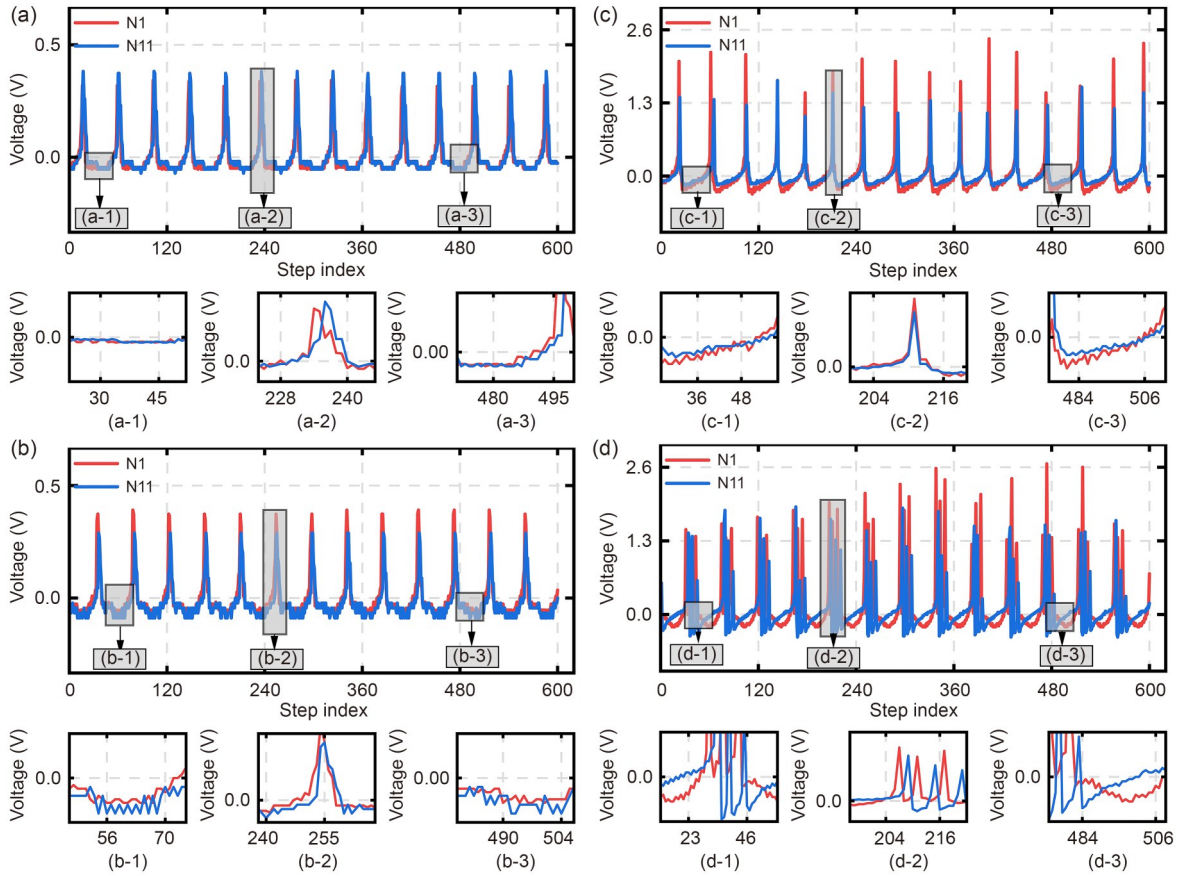

Fig. 10 Action potential diagrams of synchronous states of chain- and ring-type HH and IZH model network circuits: (a) chain-type HH model; (b) ring-type HH model; (c) chain-type IZH model; (d) ring-type IZH model. The enlarged subplots marked as (-1), (-2), and (-3) show three characteristic phases of the action potential, namely, depolarization, repolarization, and hyperpolarization, respectively

Table 3 Synchronization index and reliability indicator of the model before and after being subjected to interference

Model	Synchronization index	Reliability indicator
Chain-shaped, without interference (HH)	0.242 09	0.989 12
Ring-shaped, without interference (HH)	0.516 40	0.989 77
Chain-shaped, without interference (IZH)	0.087 67	0.810 99
Ring-shaped, without interference (IZH)	0.508 48	0.831 51
Chain-shaped, with interference (HH)	0.195 91	0.870 41
Ring-shaped, with interference (HH)	0.148 88	0.836 18
Chain-shaped, with interference (IZH)	0.396 36	0.716 15
Ring-shaped, with interference (IZH)	0.664 82	0.600 67

achieves high reliability values close to 1.0, with 0.989 12 and 0.989 77 for the chain and ring structures, respectively; the synchronization indices are 0.242 09 and 0.516 40, respectively. After introducing interference, the reliability slightly decreases to 0.870 41 and 0.836 18 for the chain and ring structures, respectively, indicating that the HH circuit maintains strong output consistency under disturbance. In contrast, the IZH model exhibits significantly lower reliability, decreasing from 0.810 99 and 0.831 51 under interference-free conditions to 0.716 15 and 0.600 67 after disturbance for the chain and ring structures, respectively.

In terms of the synchronization index, the IZH model exhibits higher sensitivity to disturbance. For the chain structure, the synchronization index increases from 0.087 67 to 0.396 36, indicating disorder-driven firing rather than stable synchronization. For the ring structure, the synchronization index increases from 0.508 48 to 0.664 82; however, this increase is accompanied by waveform distortion and phase inconsistency, as shown in Fig. 10. These results indicate that an increase in the synchronization index does not always imply improved synchronization quality but may instead reflect excessive excitation and unstable phase behavior.

4.3.4 Results of energy indicators

The quantitative results presented in Tables 4 and 5 support these observations. Under interference-free conditions, the HH model exhibits relatively close activity energy values in the chain and ring structures, with 0.005 611 and 0.006 070, respectively. After introducing interference, the activity energy slightly decreases to 0.004 633 and 0.004 940 for the chain and ring structures, respectively, indicating that the HH circuit maintains stable dynamic-state energy under disturbance. In contrast, the IZH model exhibits more significant topology-dependent variations. Under interference-free conditions, the activity energy values are 0.149 233 and 0.062 435 for the chain and ring structures, respectively. After the introduction of interference, these values decrease to 0.124 591 and 0.032 987, respectively,

Table 4 Activity energy of the model before and after being disturbed

Model	Activity energy
Chain-shaped, without interference (HH)	0.005 611
Ring-shaped, without interference (HH)	0.006 070
Chain-shaped, without interference (IZH)	0.149 233
Ring-shaped, without interference (IZH)	0.062 435
Chain-shaped, with interference (HH)	0.004 633
Ring-shaped, with interference (HH)	0.004 940
Chain-shaped, with interference (IZH)	0.124 591
Ring-shaped, with interference (IZH)	0.032 987

Table 5 Relative energy deviation of the model before and after being disturbed

Model	Relative energy deviation
Chain (HH)	0.005 611
Ring (HH)	0.006 070
Chain (IZH)	0.149 233
Ring (IZH)	0.062 435

showing that the disturbed output state of the IZH circuit is more strongly affected by topology.

In terms of energy indicators, the HH and IZH models exhibit different sensitivity levels to disturbance under chain and ring topologies. For the HH model, the activity energy decreases from 0.005 611 to 0.004 633 and from 0.006 070 to 0.004 940 in the chain and ring structures, respectively, indicating small variations before and after interference. The corresponding relative energy deviations are 0.174 300 and 0.186 161, respectively, demonstrating that disturbance causes limited dynamic-state deviation in the HH circuit and that the two topologies preserve a similar dynamic-state level under disturbance. In contrast, the IZH model exhibits significantly stronger topology-dependent variations. For the chain structure, the activity energy decreases from 0.149 233 to 0.124 591, with a relative energy deviation of 0.165 124, which is close to that of the HH model. However, for the ring structure, the activity energy decreases significantly from 0.062 435 to 0.032 987, and the relative energy deviation increases rapidly to 0.471 659, indicating that the disturbed dynamic state departs significantly more strongly from the undisturbed dynamic state. These results suggest that the HH circuit exhibits stronger dynamic-state preservation under disturbance, whereas the IZH circuit is more sensitive to interactions between neuronal dynamics and network topology.

4.4 Discussion of the experimental anti-interference performance

From the perspective of circuit implementation, the HH neuron is achieved using multiple parallel computation paths composed of multipliers, adders, LUTs, and control logic. The gating variables m, h, and n are generated using LUTs or exponential approximations to obtain the corresponding α and β parameters, followed by numerical integration using multiplier and adder chains. This multi-branch structure enables parallel computation of sodium, potassium, and leakage currents, forming a multipath feedback system. In contrast, the IZH neuron contains only two state variables, namely, membrane potential V and recovery variable U, and its computation is implemented using a simpler multiplier and adder structure. Synaptic coupling is achieved through linear operations, resulting in a simplified feedback path.

This structural difference directly determines the synchronization, anti-interference capability, and energy-state preservation of the circuit. In the HH implementation, the presence of multiple feedback paths allows disturbances to be absorbed across different temporal scales. Each computational branch contributes to correcting phase deviations and buffering disturbance-induced dynamic variations, enabling the system to rapidly return to a stable oscillatory trajectory. This explains why both ring and chain HH circuits maintain high synchronization and reliability. From the perspective of energy indicators, the HH circuit also exhibits relatively small variations in activity energy and limited relative energy deviation after interference injection, indicating that its original dynamic state is effectively preserved under disturbance.

In contrast, the IZH circuit relies on a single feedback mechanism and operates on a single time scale. Consequently, it lacks the ability to dissipate disturbance energy progressively. The ring structure partially compensates for phase deviations through cyclic feedback; however, recovery remains limited. The chain structure, without feedback, accumulates errors along the propagation path, resulting in delayed and irregular firing in downstream neurons. From the perspective of energy indicators, the IZH circuit exhibits stronger topology-dependent dynamic-state variations under disturbance. In particular, the relative energy deviation of the ring-type IZH circuit is significantly greater than that of the chain-type structure, indicating that the disturbed dynamic state departs more strongly from the undisturbed dynamic state.

Overall, the experimental results demonstrate that the HH circuit provides stronger hardware-level anti-interference capability, synchronization stability, and dynamic-state preservation, whereas the IZH circuit is more sensitive to disturbance and highly dependent on network topology. These findings are consistent with the simulation results presented in Section 3.

This section maps complex neural dynamics models onto FPGA-based digital circuits, proposing an efficient TDM IP deployment framework. Comparative analysis between the HH and IZH models reveals that the HH network offers superior synchronization stability, reliability, and energy-state preservation at the cost of higher resource consumption. In contrast, the IZH network exhibits excellent computational efficiency and scalability for large-scale neural implementations but shows higher sensitivity of the dynamic state to structured disturbance. These hardware verifications provide engineering foundations for real-time bio-inspired computation, neural modulation, and interference-resistant circuit design.

5 Conclusions

This study investigates the anti-interference stability and hardware feasibility of bio-inspired neural synchronous discharge circuits based on HH and IZH models. The results demonstrate that HH networks exhibit stronger robustness, better synchronization stability, and faster rhythm recovery under structured disturbances, primarily because of their multichannel gated feedback and biophysical dynamic

regulation. In contrast, IZH networks require fewer hardware resources and offer higher implementation efficiency; however, their synchronization stability is more easily degraded under interference. The comparison of network topologies also indicates that small-world structures improve synchronization maintenance through multipath phase coordination, whereas chain structures are more susceptible to cumulative disturbance propagation. The FPGA implementation verifies that neural synchronization mechanisms can be effectively incorporated into digital hardware. Overall, this study demonstrates the feasibility of introducing biological synchronization dynamics into engineered adaptive anti-interference circuit design.

Supplementary information

The online version contains supplementary materials available at https://doi.org/10.1631/ENG.ITEE.2026.0117.

Acknowledgments

This work was supported by the National Natural Science Foundation of China (No. 62401478), the Youth Fund Project of Sichuan Province (No. 2025ZNSFSC1436), and the Innovation Team Project (No. KCXTD2024-2).

Author contributions

Chaojun CHEN designed the research methodology and drafted the paper. Shutong CHEN performed the simulations and analyzed the data. Yun MA carried out the hardware implementation. Junxi ZHU processed the data. Chenxi ZHAO validated the results. Quanlin GUO provided resources and helped organize the paper. Dezhi GOU supervised the research, acquired funding, and revised and finalized the paper.

Conflict of interest

All the authors declare that they have no conflict of interest.

Data availability

The data that support the findings of this study are available from the corresponding author upon reasonable request.

Declaration on the use of generative AI tools

During the preparation of this work, the authors used ChatGPT to improve language. After using this tool, the authors reviewed and edited the content as needed and take full responsibility for the content of the published article.

References

Beaubois R, Cheslet J, Ikeuchi Y, et al., 2024. Real-time multicompartment Hodgkin-Huxley neuron emulation on SoC FPGA. *Front Neurosci*, 18:1457774. https://doi.org/10.3389/fnins.2024.1457774

Bossy M, Fontbona J, Olivero H, 2019. Synchronization of stochastic mean field networks of Hodgkin–Huxley neurons with noisy channels. *J Math Biol*, 78(6):1771-1820. https://doi.org/10.1007/s00285-019-01326-7

Guo L, Song YH, Wu YX, et al., 2023. Anti-interference of a small-world spiking neural network against pulse noise. *Appl Intell*, 53(6):7074-7092. https://doi.org/10.1007/s10489-022-03804-w

Heidarpur M, Ahmadi A, Ahmadi M, 2024. The silence of the neurons: an application to enhance performance and energy efficiency. *Front Neurosci*, 17:1333238. https://doi.org/10.3389/fnins.2023.1333238

Hodgkin AL, Huxley AF, 1952. A quantitative description of membrane current and its application to conduction and excitation in nerve. *J Physiol*, 117(4):500-544. https://doi.org/10.1113/jphysiol.1952.sp004764

Izhikevich EM, 2003. Simple model of spiking neurons. *IEEE Trans Neur Netw*, 14(6):1569-1572. https://doi.org/10.1109/TNN.2003.820440

Kazemi S, Jamali Y, 2022. Phase synchronization and measure of criticality in a network of neural mass models. *Sci Rep*, 12(1):1319. https://doi.org/10.1038/s41598-022-05285-w

Khoshkhou M, Montakhab A, 2020. Explosive, continuous and frustrated synchronization transition in spiking Hodgkin–Huxley neural networks: the role of topology and synaptic interaction. *Phys D*, 405:132399. https://doi.org/10.1016/j.physd.2020.132399

Lin PL, Liao ZS, Chen SM, et al., 2025. Achieving neuronal dynamics with spike encoding and spatial-temporal summation in vanadium-based threshold switching memristor for asynchronous signal integration. *Nanoscale Horiz*, 10(2):379-387. https://doi.org/10.1039/d4nh00484a

Liu DH, Sugawara R, Hanioka S, et al., 2023. EMI mitigation using a learning-based frequency modulation carrier in PWM inverters. Proc 49th Annual Conf of the IEEE Industrial Electronics Society, p.1-6. https://doi.org/10.1109/IECON51785.2023.10312081

Liu SH, Ma GL, Man MH, et al., 2022. Research progress of electromagnetic protection biomimetics. *High Volt Eng*, 48(5):1750-1761 (in Chinese). https://doi.org/10.13336/j.1003-6520.hve.20211940

Ma J, 2023. Biophysical neurons, energy, and synapse controllability: a review. *J Zhejiang Univ-Sci A*, 24(2):109-129. https://doi.org/10.1631/jzus.A2200469

Mainen ZF, Sejnowski TJ, 1995. Reliability of spike timing in neocortical neurons. *Science*, 268(5216):1503-1506. https://doi.org/10.1126/science.7770778

Peng HH, Gan L, Guo X, 2024. Memristor-based spiking neural networks: cooperative development of neural network architecture/algorithms and memristors. *Chip*, 3(2):100093. https://doi.org/10.1016/j.chip.2024.100093

Savtchenko LP, 2007. Bilateral processing in chemical synapses with electrical 'ephaptic' feedback: a theoretical model. *Math Biosci*, 207(1):113-137. https://doi.org/10.1016/j.mbs.2006.09.016

Schuman CD, Kulkarni SR, Parsa M, et al., 2022. Opportunities for neuromorphic computing algorithms and applications. *Nat Comput Sci*, 2(1):10-19. https://doi.org/10.1038/s43588-021-00184-y

Soltani R, Benmohamed E, Ltifi H, 2024. Newman-Watts-Strogatz topology in deep echo state networks for speech emotion recognition. *Eng Appl Artif Intell*, 133:108293. https://doi.org/10.1016/j.engappai.2024.108293

Takahashi S, Wada K, Ayano H, et al., 2022. Review of modeling and suppression techniques for electromagnetic interference in power conversion systems. *IEEJ J Ind Appl*, 11(1):7-19. https://doi.org/10.1541/ieejjia.21006800

Wang B, Zhang XY, Wang SC, et al., 2025. Topology optimization of random memristors for input-aware dynamic SNN. *Sci Adv*, 11(16):eads5340. https://doi.org/10.1126/sciadv.ads5340

Wang XQ, Yu D, Wu Y, et al., 2023. Effects of potassium channel blockage on inverse stochastic resonance in Hodgkin-Huxley neural systems. *J Zhejiang Univ-Sci A*, 24(8):735-748. https://doi.org/10.1631/jzus.A2200625

Wu XG, Gao XJ, Wang JL, et al., 2023. Advances in modeling and suppression methods of EMI in power electronic converters of third-generation semiconductor devices. *Electronics*, 12(11):2348. https://doi.org/10.3390/electronics12112348

Yu XH, Bao H, Chen M, et al., 2023. Energy balance via memristor synapse in Morris-Lecar two-neuron network with FPGA implementation. *Chaos Sol Fract*, 171:113442. https://doi.org/10.1016/j.chaos.2023.113442

Yuan L, Zhang J, Liang Z, et al., 2023. EMI challenges in modern power electronic-based converters: recent advances and mitigation techniques. *Front Electron*, 4:1274258. https://doi.org/10.3389/felec.2023.1274258

Zhang YZ, Zhou CL, Bao H, et al., 2026. A heterogeneous cyclic Hopfield neural network without self-connections. *J Zhejiang Univ-Sci A*, 27(3):306-316. https://doi.org/10.1631/jzus.A2500350

Zhao YJ, Xiao LF, Liu YL, et al., 2024. Electromagnetic interference elimination via active sensing and deep learning prediction for radiofrequency shielding-free MRI. *NMR Biomed*, 37(7):e4956. https://doi.org/10.1002/nbm.4956

Zhou P, Ma J, Xu Y, 2023. Phase synchronization between neurons under nonlinear coupling via hybrid synapse. *Chaos Sol Fract*, 169:113238. https://doi.org/10.1016/j.chaos.2023.113238